A Segmentation and Reconstruction Technique for 3D Vascular Structures

Vincent Luboz[1], Xunlei Wu[1], Karl Krissian[2], Carl-Fredrik Westin[2], Ron Kikinis[2], Stéphane Cotin[1], and Steve Dawson[1]

[1] The SIM Group – CIMIT/ MGH, 65 Landsdowne Street, Cambridge, MA 02139, USA
{vluboz, xwu4, scotin, sdawson}@partners.org
http://www.medicalsim.org/index.htm
[2] SPL, Brigham and Women's Hospital, 75 Francis Street, Boston, MA 02115, USA
{karl, westin, kikinis}@bwh.harvard.edu
http://splweb.bwh.harvard.edu:8000/

Abstract. In the context of stroke therapy simulation, a method for the segmentation and reconstruction of human vasculature is presented and evaluated. Based on CTA scans, semi-automatic tools have been developed to reduce dataset noise, to segment using active contours, to extract the skeleton, to estimate the vessel radii and to reconstruct the associated surface. The robustness and accuracy of our technique are evaluated on a vascular phantom scanned in different orientations. The reconstructed surface is compared to a surface generated by marching cubes followed by decimation and smoothing. Experiments show that the proposed technique reaches a good balance in terms of smoothness, number of triangles, and distance error. The reconstructed surface is suitable for real-time simulation, interactive navigation and visualization.

1 Introduction

Stroke is a leading cause of death. Our team is developing a real-time neuro-interventional radiology simulation system where physicians will be able to learn and practice without putting patients at risk. This kind of application requires a streamlined data processing from a patient's computer tomography angiogram (CTA) to a computer representation of the vasculature. Therefore, the reconstructed vascular network has to be *smooth* for visualization, *structured* for blood flow computation, and *efficient* for real time collision detection/collision response between interventional tools and vessel wall. The method presented in this paper generates virtual vasculature through segmentation and surface reconstruction.

Current techniques for processing vascular images can be divided in two main approaches: techniques for centerline enhancement, including multi-scale approaches, usually based on the Hessian matrix; and techniques for contour extraction, including statistical approaches: Expectation Maximization [1], random Markov fields, and geometrical approaches: region growing, adaptive thresholding, active contours that can be explicit, like snakes, or implicit, like level sets [2, 3]. These techniques usually perform better after noise reduction. A topological representation of the vascular network can be obtained from both approaches either by computing ridges or by applying a thinning technique like homotopic skeletonization.

J. Duncan and G. Gerig (Eds.): MICCAI 2005, LNCS 3749, pp. 43 – 50, 2005.

The result of the segmentation is then processed to generate an efficient and structured representation of vascular structure for our purpose. Bühler et al. [4] presents a comprehensive and up-to-date survey on surface reconstruction techniques. Our surface reconstruction algorithm improves upon [5] in that the coarse base mesh generation is followed by smoothing through surface subdivision. The base mesh and multiscale subdivision approach, as shown in subsequent sections, is proved to be a robust framework for real-time physics-based flow computation, smooth tissue/tool interaction, as well as high-fidelity anatomical visualization.

Section 2 will describe our semi-automatic tools which reduce dataset noise, segment using active contours, compute the skeleton, estimate the vessel radii and reconstruct the associated surface. In section 3, we present different tests performed on the phantom and used to evaluate the robustness and the accuracy of our method. Finally, discussion and conclusion are presented in the last section.

2 Materials and Method

Our process consists in the following pipeline: anisotropic diffusion, level set evolution, skeletonization, pruning, connection and smoothing, radius estimation, reconstruction. This approach preserves the topology at junctions and gives semi-automatically a skeleton requiring little interaction before surface reconstruction.

2.1 Segmentation

The first step of the segmentation is to apply an anisotropic diffusion filter based on [6]. This filter reduces the noise while preserving small vascular structures enabling better segmentation which is important in the region of the brain. Next, we remove the skull bones, the sinuses and the skin, who the similar intensity as the vessels and might disturb the segmentation process, using morphological operations.

We then segment the vessel contours by the means of a level set evolution. For efficiency, we initialize the active contour using a threshold on the image intensity. The level set equation [7, 2], evolves a surface according to three different forces: an advection force that pushes the surface towards the edges of the image, a smoothing term that keeps the surface smooth and a balloon force that allows expansion of the contours within vascular structures. The smoothing term is proportional to the minimal curvature of the surface [8]. The balloon force relies on the intensity statistics to either expand or shrink the evolving contour. This force is expressed as $exp(-(I-m)^2/\sigma^2)-\tau$ where I is the intensity, m stands for the mean intensity of the vessels, σ is their standard deviation, and τ is a threshold (0.2 by default) that allows shrinking the contour when the position is unlikely to belong to a vessel. A 3D model of the vessels is obtained as the iso-surface of intensity zero from the result of the level set evolution, using the Marching-Cubes algorithm [9]. From the result of the level set, a skeletonization technique is applied to obtain a simple topological representation of the vascular network. It is based on homotopic thinning where voxels are removed in the order of the Euclidean distance to the segmented surface. Voxels are iteratively removed if they are simple [10] and if they are not end-points, such that they have more than one neighbor in a 3x3x3 neighborhood.

After the skeletonization, small vessels can still have connectivity discrepancies along the centerlines near small branches. Consequently, a pruning is applied to remove small leaves (lines with at least an extremity which is not a junction). We then connect the lines that are close but disconnected because of the resolution of the medical dataset. This connection is made only if the lines are close to each other and their directions are matching within a small difference, which could be induced by the vessel curvature. At this step, some manual work is often needed. This work consists in connecting lines that are too far to be connected automatically or in removing lines that are too long to be deleted.

Once the connected skeleton is finished, the radius of the lines is extracted from the dataset. This is done using the intensity gradient in the binary image obtained from the level set evolution. Starting from the centerline, we grow a circle in the plan of the cross-section and stop when there is a relevant local maximum of the intensity gradient, thus giving estimated radii along the centerlines.

2.2 Surface Reconstruction

The goal of our surface reconstruction is to generate a smooth surface that can be easily refined to suit the needs of efficient collision detection/response, stable vessel deformation, real-time flow simulation, also multi-scale anatomical visualization. Our algorithm improves over [5] in four main areas:

1. Handling directed graphs with loops and multiple roots.

One branch is allowed to have multiple parents and children. Artery vessels can form loops, e.g. circle of Willis. *One branch can connect to a single branch forming 1-furcation.* This is useful to construct a unified directed graph for both artery and venous sides. *Multiple trees can be reconstructed at the same time*.

2. Trunk branch selection based on angle and radii variance.

Fig. 1. *Left:* Trunk branch selection: using both vessel average radii and branching angle to determine the continuation trunk branch. Although $\theta_j < \theta_i$, B_1^{in} is chosen as the trunk branch of B_0^{in}, due to the similarity of their average radii. *Middle:* Cross section distribution gets denser at thinner regions of a vessel. *Right:* the density is higher where a vessel turns or twists.

To patch the surface at vessel joints, both algorithms define at a trunk branch with respect to the current branch and form polygons to connect the trunk surface and other joint branches base meshes. Since n_i, the cross section normal at the beginning or end of branch B_i, is computed by differentiating neighboring sampling points, the approximation can be misleading when centerlines are under sampled. Our scheme considers both branching angle and vessel radii to reduce under-sampling artifacts which improves the reconstruction robustness. First, n_i^{in} where $i>0$ are reversed. Then, we com-

pute the disparity $\Omega_i \equiv \lambda\ \theta_i + (1-\lambda)\,/r_i - r^{in}{}_0/$, where $\lambda \in [0,1]$ is the weight balancing the influence of branching angle and of the average radii variance. The algorithm picks the branch with minimal Ω as the trunk branch. In the left half of Fig. 1, although $\theta_j < \theta_i$, $B_1{}^{in}$ is chosen due to the similarity of their average radii.

3. Adaptive cross sections distribution.

Our cross section distribution scheme (2) considers radii and centerline curvature:

$$x_{i+1} - x_i = \alpha\left(\frac{r_{i+1}}{1+\beta\kappa_{i+1}} + \frac{r_i}{1+\beta\kappa_i}\right) \qquad i \in [0, N_{segment} - 1] \tag{2}$$

where x_i is the curvilinear coordinate of the cross section center. r_i and κ_i [11] are the corresponding radius and Gaussian curvature, respectively, obtained by linear interpolation between two adjacent raw skeleton samples where $\alpha>0$ is the desired spacing scalar and $\beta>0$ is the weight on curvature influence. Eq. (2) states that after filtering, the centers of two adjacent cross sections are placed closer if the vessel is thin or turns. A straight branch does not need many cross sections to resemble its original geometry. Assembling (2) for all i yields $(N_{seg}-1)$ nonlinear algebraic equations with $(N_{seg}-1)$ unknowns, since x_0 and x_N are set to be the curvilinear coordinates of the vessel end nodes. Broyden's method [12] is used to solve for all x_i.

4. Robust joint tiling: *end-segment-grouping* and *adjacent-quadrant-grouping*.

We connect every branch to its trunk using both end segments regardless the branching angles so that a single recursive joint tiling is needed. *End-segment-grouping*, unifies all the outgoing branches together such that the *connecting patches* connect the bottom of the outgoing branch's base mesh with both end segments of the trunk branches, i.e. *Seg(N-1)* and *Seg(0),* demonstrated in the left half of Figure 2.

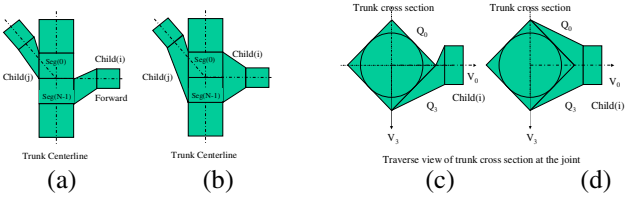

Fig. 2. (a) Felkel's method connects forward *Child(j)* to *Seg(0)* and backward *Child(i)* to *Seg(N-1)*. (b) *End-segment-grouping* connects *Child(i)* and *Child(j)* both *Seg(N-1)* and *Seg(0)*. The bottle-neck effect is reduced. When *Child(i)* lies close to the boundary of Q_3, (d) *adjacent-quadrant-grouping* uses both Q_0 and Q_3 eliminates twisting artifact by using only Q_3 in [5] (c).

When the outgoing centerline forms a small angle with the trunk centerline, using single end segment produces bottle-neck effect. The artifact is reduced when both end segments are deployed for the joint tiling. When the outgoing centerline lies in or close to the bisection plane of two trunk centerlines, using a single end segment loses the symmetry. This symmetry is nicely preserved by connecting the mesh of *Child(i)* to the same sides of *Seg(N-1)* and *Seg(0). End-segment-grouping* not only reduces the patching artifacts in both extreme cases, but yields smoother trunk-to-branch transition under all branching configuration.

We improve the joint tiling not just in the trunk centerline direction. *Adjacent-quadrant-grouping* is designed to use 2 adjacent sides of the end hexahedron seg-

ments. When a child centerline lies close to the boundary of 2 quadrants, tiling with only one quadrant introduces twists. This artifact is eliminated by adding the neighboring quadrant into the tiling, e.g. Q_0 and Q_3 are grouped together as a whole when tiling *Child(i)* to the trunk mesh. When *Child(i)* lies close to a quadrant center, our approach uses only current quadrant for the tiling as in [5].

With these improvements, the proposed reconstruction scheme is able to handle more general directed graph. It is less prone to artifacts due to initial data sampling. It is also more robust to present full range of bifurcation configuration. The reconstructed smooth vascular surface is suitable for the purpose of efficient and stable physics modeling, and smooth visualization.

3 Tests and Evaluation

Our vascular phantom, in Fig. 3(a), is composed of a Plexiglas box filled with silicon gel and nylon tubing forming a simplified vasculature. Vessel radii range from *0.78mm* (simulating small brain vessels) to *2.34mm* (simulating the middle cerebral artery). After CTA scans of the phantom, the segmentation leads to a skeleton from which the reconstruction module generates a smooth surface as shown in Fig. 3(b).

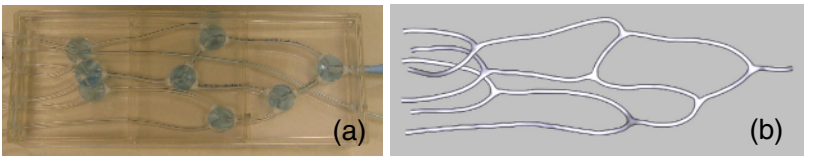

Fig. 3. *(a)* The silicon phantom with nylon tubing. *(b)* Reconstruction of the 3D surface

To evaluate the rotational invariance and robustness of our method, we scanned this phantom in *12* different orientations. The phantom orientations are obtained via a *45°* or *90°* rotation on one or more axes. The CTA scan resolution is 0.6 x 0.6 x 1.25 mm.

3.1 Evaluation of the Robustness of the Vessel Lengths and Radii

The segmentation method, described in section 2, was applied to those datasets with following parameters: *1000* level set iterations; using intensity threshold of *2300* with standard deviation (SD) of *750*; *5mm* pruning; *2mm* maximal distance for gap connection; radius estimation with gradient computed from the derivatives of a Gaussian kernel with SD *0.4mm*. Line orientation was manually corrected before the final surface reconstruction (Fig. 3(b)). To evaluate the results, the lengths and the radii have been analyzed through the Brand-Altman method [13]. Fig. 4 shows that length variation stays within *1.0mm, while 2 σ length=3.5mm*. In only 6 out of 204 cases (17tubes x 12scans), the radius variation is out of [*-2 σ radius, 2 σ radius*], where *2 σ radius=0.2mm*.

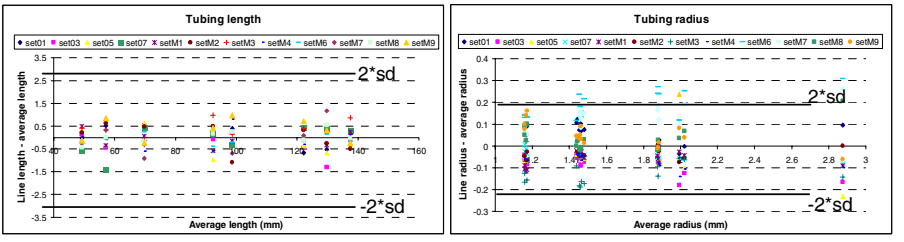

Fig. 4. Brand-Altman plots for (a) the tube lengths and (b) the average radii. The upper and the lower limits represent *2 σ*. Very few length and radius values are away from their average.

3.2 Evaluation of the Mesh Accuracy and Smoothness

We measure surface smoothness and the distance between two surfaces. *Hausdorff* distance is computed using MESH software[1]. Smoothness is measured as the RMS of the minimal and the maximal surface curvatures, κ_1 and κ_2 respectively. They are computed by fitting a 2nd polynomial to each vertex and its direct neighbors: using this small region considers the surface noise in the smoothness measure. The lower the value, the smoother the surface is. Fig. 5(a) depicts the distance between our reconstructed model at 3 subdivision levels, L_0, L_1, L_2 and the surface, S_0, obtained from the Marching Cubes algorithm applied to the result of the level set segmentation. The RMS is always less than one voxel (*<0.6mm*) and lower than *0.4mm* on L_1.

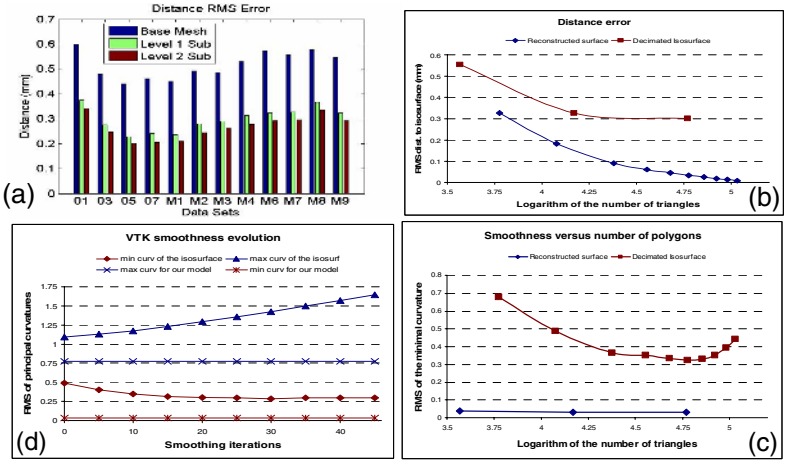

Fig. 5. (a) Root Mean Square (RMS) distance error for 12 data sets at 3 subdivision. (b) RMS distance error on M7 versus the number of triangles, after different decimations of the original iso-surface. (c) RMS of the min curvature, versus the number of triangles. (d) Smoothness evolution for different smoothing levels compared to the smoothness our model at level 1.

[1] http://mesh.berlioz.de

We compared the smoothness and the distance error on M7 obtained from our reconstruction to the ones obtained using the VTK[2]. Fig. 5(b) shows the distance between S_0 and L_0, L_1, L_2 compared to the distance between S_0 and its decimations S_0^d, $d \in [0,9]$ using *vtkDecimatePro*. The RMS after decimation is always smaller, because most errors occur at vessel extremities or junctions. However, our model allows simpler mesh, with reasonable error ($RMS<0.6mm$) and good smoothness shown in Fig. 5(c). This figure displays the RMS of κ_1 on L_0, L_1, L_2 and on S_0^d. It is almost constant (0.03) for all levels and much better than any S_0^d (between *0.3* and *0.7*). For completeness, we also depict the RMS of κ_1 and κ_2 for L_1 and S_0^8 having similar number of triangles. Fig. 5(d) plots the evolution of these smoothness measures according to the number of smoothing iterations, where we smooth S_0^8 by applying the *vtkSmoothPolyDataFilter*. The RMS of κ_2 always increases with the smoothing due to vessel shrinkage, and the RMS of κ_1 decreases to *0.25* while L_1 have a value of 0.03. This shows our model smoothness superiority over VTK smoothing.

3.3 Results on a Clinical Dataset

Before evaluating on a full clinical dataset, we apply our method to a portion of a patient vascular network in Fig. 6(a). The testing data contains the end of the vertebral arteries, joining into the basilar artery which then split into the posterior cerebral arteries. A local level set, ignoring the small vessels, followed by an iso-surface reconstruction allowed getting those arteries shown in Fig. 6(b). After skeletonization and surface reconstruction shown in Fig. 6(c), both surfaces are compared. Fig. 6 (b) shows the color code of the distance between the two surfaces. The RMS distance error is lower than *0.4mm* with 5% of iso-surface triangles. The result of our streamlined process, on a full CTA dataset, is depicted in Fig. 6(d).

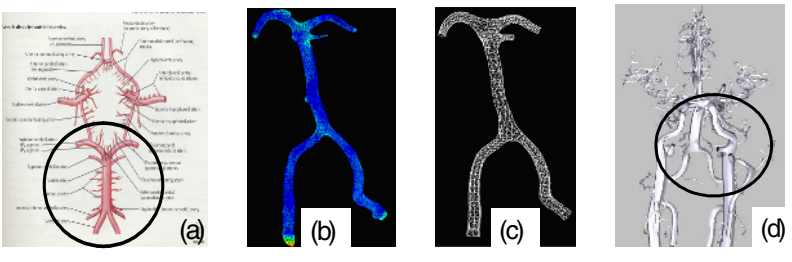

Fig. 6. (a) Anatomy of the circle of Willis; (b) segmented iso-surface; (c) reconstructed surface. The color code in (b) ranges from blue (0.0mm) to red (3.0mm), (d) reconstructed arterial side.

4 Discussion and Conclusion

The method presented in this article deals with the segmentation and the reconstruction of the vascular network. The final reconstructed vascular surface is aimed to be integrated in a neuro vascular training and procedural planning simulator. The goal of our method is to streamline the process from the CTA scan of a patient to a structured,

[2] Visual Tool Kit library available at http://www.vtk.org

smooth, and efficient vascular model with minimum manual interactions. It has shown interesting results in term of accuracy and robustness. Indeed, its evaluation on the phantom in 12 different orientations produces homogeneous skeletons and radii. The generated surfaces are close to the reference ones and are much smoother. The main drawback of our method is that it is not fully automatic and it estimates circular vessel cross sections.

In future work, the main effort will focus on reducing the amount of manual work. On the segmentation side, one main difficulty is to separate tangent vessels, which are merged at the current imaging resolution. Another difficulty is to fully detect small vessels. Both tasks would benefit from an a priori knowledge based on an anatomical atlas. As a perspective, we would like to integrate a labeling tool in the skeletonization step. This feature could give the name of the arteries and veins and consequently help in the training/learning process of our simulator. An automatic correction of centerline orientation is also under investigation based on graph theory. For the estimation of the cross-sections, fitting an ellipse instead of a circle would help to match their real geometry without sacrificing the smoothness and the low complexity of the mesh. Finally, testing the whole method on more patients would help to validate it on large scale networks before integrating it in the neuro-vascular intervention training system mentioned above.

References

1. Wells, W. M. and Grimson, W. E. L. and Kikinis, Ron and Jolesz, Ferenc A. Adaptive Segmentation of MRI Data Springer-Verlag, 1995 , 905 , 59-69.
2. Sethian, J.A. Level Set Methods and Fast Marching Methods: Evolving Interfaces in Comp. Geom., Fluid Mech., Comp. Vision and Materials Sci. Cambridge Univ. Press, 1999.
3. Suri, J.S., Liu, K., Singh, S., Laxminarayan, S.N., Zeng, X., Reden, L.: Shape recovery algorithms using level sets in 2D/3D medical imagery: a state-of-the-art review IEEE Transactions on Information Technology in Biomedicine, 2002 , 6 , 8-28.
4. Bühler, K., Felkel, P., La Cruz, A.: Geometric Methods for Vessel Visualization and Quantification - A Survey. VRVis Research Center, Austria, 2002, Technical Report, pp. 24-48.
5. Felkel, P., Wegenkittl, R., Bühler, K.: Surface Models of Tube Trees. In: Computer Graphics International (CGI'04), pp. 70-77.
6. Krissian, Karl Flux-based anisotropic diffusion applied to enhancement of 3-D angiogram. IEEE Trans Med Imaging, 2002, 21 , 1440-2.
7. Osher, S., Sethian, J.A. Fronts propagating with curvature dependent speed: algorithms based on the Hamilton-Jacobi formalism J. Comput. Physics, 1988 , 79 , 12-49.
8. Lorigo, L.M., Faugeras, O.D., Grimson, W.E.L., Keriven, R., Kikinis, R., Nabavi, A., Westin, C.-F. CURVES: Curve Evolution for Vessel Segm. MedIA, 2001 , 5 , 195-206.
9. Lorensen, W.E., Cline, H.E. Marching Cubes: A high resolution 3-D surface construction algorithm Computer Graphics, 1987, 21, 163-169.
10. Malandain, G., Bertrand, G., Ayache, N. Topological Segmentation of Discrete Surfaces IJCV, 1993 , 10 , 183-197.
11. Calabi, E., Olver, P.J., Shakiban, C., Tannenbaum, A., Haker, S.: Differential and Numerically Invariant Signature Curves Applied to Object Recognition. IJCV, 1998 (26):107-35.
12. Press, W.H., Teukolsky, S.A., Vetterling, W.T., Flannery, B.P.: Numerical Recipes in C, University Press, Cambridge, 1992.
13. Bland, J.M., Altman, D.G.: Statistical methods for assessing agreement between two methods of clinical measurement. *Lancet*, i: 307-310, 1986.